Top Med Chem (2020) 34: 55–80
DOI: 10.1007/7355_2019_85

Published online: 28 January 2020

Inorganic Fluorescent Nanomaterials

Taeho Kim and Jesse V. Jokerst

Contents

Abstract Optical imaging is a noninvasive imaging technology to visualize the specific biological processes by detecting the emissive photons under external energy excitation. In particular, inorganic nanomaterials have attracted great attention as exogenous fluorescent probes for optical imaging due to their superiority in imaging sensitivity, systemic circulation, target specificity, and versatility in chemical design for theranostic purposes. This book chapter comprehensively summarizes the recent advances in inorganic fluorescent nanomaterials, including quantum dots, upconversion, metal nanoclusters, and carbon-based and silicon-based nanomaterials. It will be reviewed in detail the fluorescence mechanism of the

T. Kim (✉)
Department of NanoEngineering, University of California San Diego, La Jolla, CA, USA

Department of Biomedical Engineering, Michigan State University, East Lansing, MI, USA

Institute for Quantitative Health Science and Engineering, Michigan State University, East Lansing, MI, USA
e-mail: kimtae47@msu.edu

J. V. Jokerst (✉)
Department of NanoEngineering, University of California San Diego, La Jolla, CA, USA

Materials Science Program, University of California San Diego, La Jolla, CA, USA

Department of Radiology, University of California San Diego, La Jolla, CA, USA
e-mail: jjokerst@ucsd.edu

nanomaterials based on their optical excitations, the current utility in high-resolution (preclinical) in vivo imaging, and the underlying issues for future clinical translations.

Keywords Fluorescence, In vivo, Molecular imaging, Nanomaterials, Optical imaging, Quantum dots

1 Overview

Most clinical optical imaging agents are organic fluorescent dyes (e.g., cyanine, rhodamine, oxazine dyes). However, these suffer from several drawbacks such as photo-bleaching and short blood circulation, which limit their repeated use for long-term imaging of cellular and molecular processes in living systems. In the last two decades, many efforts have been devoted to developing inorganic (metal-containing) nanoparticles as targetable optical probes with superior photostability. In this chapter, we will discuss several types of inorganic nanoparticles that use fluorescence. We will also introduce some recent studies to validate their interesting features as contrast agents in preclinical in vivo imaging. Finally, we will address the potential issues for each type of fluorescent nanomaterials to attain better sensitivity and lower toxicity for potential clinical translations.

2 Quantum Dots

Quantum dots (QDs; semiconductor nanoparticles) are composed of II–VI, III–V, and IV–VI group elements of the periodic table and are representative inorganic fluorescent nanomaterials (CdSe, CdS, CdTe, ZnS, InP, InAs, etc.). Their fluorescence is induced from the quantum confinement effect, which occurs when the QD radius is smaller than the exciton Bohr radius (5.3 nm) of the original material [1].

QDs have many photo-physical advantages. QDs display narrower emission bands than the traditional organic fluorophores. QDs have high photostability that preclude the fast quenching of emissive light after repeated, high-intensity light excitations. Therefore, these highly bright and photostable QDs offer fluorescence imaging of live cells and in vivo animal imaging for long time periods [2]. QDs have multiplexed imaging for simultaneous detection of multiple distinctive biological species due to their unique size-dependent light emission [3]. This is because QDs follow the quantum behaviors of a particle in a box (the smaller the box is, the larger is the separation between energy levels); for example, while the larger CdSe QDs (5–6 nm) emit red light (relatively long wavelength), smaller CdSe QDs (2–3 nm) have blue-shifted (short) emission (higher photon energies)

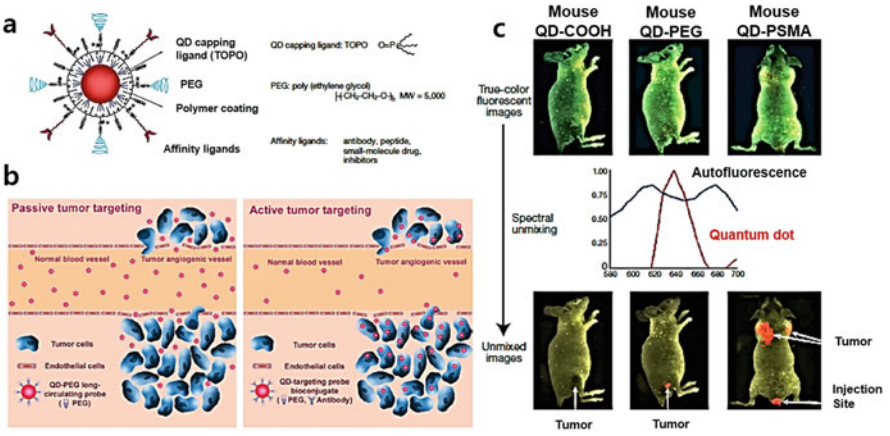

Fig. 1 Schematic illustration of QD probes for in vivo cancer targeting and imaging. (**a**) Multilayered structure of QDs, consisting of the capping ligand trioctylphosphine oxide (TOPO), encapsulating polymer layer, tumor-targeting ligand (e.g., peptides, antibodies, or small molecules), and polyethylene glycol (PEG). (**b**) Tumor targeting by enhanced permeation and retention (EPR) of QD probes via leaky tumor vasculatures (passive tumor targeting; left) or high affinity binding of QD-antibody conjugates to tumor antigens (active tumor targeting; right). (**c**) In vivo fluorescence images using QD probes with three different surface coatings with carboxylic acid groups (QD-COOH; left), PEG groups (QD-PEG; middle), and PSMA antibody conjugates (QD-PSMA; right). For all three QDs, a color image (top), two fluorescence spectra from QD and animal skin (middle), and a wavelength-resolved spectral image (bottom) were obtained from the live mouse bearing C4-2 human prostate tumors (0.5–1.0 cm in diameter) after systemic intravenous administrations of each QD. Adapted from Gao et al. [5] with permission

[4]. Remarkably, both of these systems can still utilize the same ~400 nm excitation.

Consequently, by capitalizing on the striking optical features of QDs (e.g., stale and sharp emission, spectral nature of emitted photons), Nie and coworkers reported the first study of QDs for targeting and spectral optical imaging in animal models [5]. In this study, ZnS-capped CdSe QDs were synthesized and subsequently conjugated with targeting ligands for tumor antigen recognition and polyethylene glycol (PEG) molecules for improved blood circulation (Fig. 1a). Here, the experimental groups included three different QDs with carboxylic acid groups (QD-COOH), PEG groups (QD-PEG), and prostate-specific membrane antigen (QD-PSMA). Next, each QD was intravenously injected into mice bearing human C4-2 prostate cancer xenografts (0.5–1.0 cm in diameter), and the in vivo fluorescence imaging was performed with wavelength-resolved spectral imaging. The fluorescence spectrum of the QD and the animal skin is shown in Fig. 1c. The autofluorescence spanned a broad range of wavelengths (580–700 nm), but the as-prepared QDs had a characteristic sharp emission band near 640 nm.

The authors also found that the surface-modified QD probes can be accumulated at tumors either by the enhanced permeability and retention (EPR) via leaky tumor vasculatures (passive targeting) [6, 7] or by antibody binding to cancer-specific cell

surface biomarkers (active targeting) (Fig. 1b) [8]. Figure 1c (bottom) shows no tumor signals detected with QD-COOH (no specific targeting), and the only weak signals were observed for QD-PEG (passive targeting); however, very intense signals were detected for QD-PSMA (active targeting). These results indicate the active tumor targeting is more efficient than passive targeting [5].

Since this groundbreaking work, there have been studies to show the surface-modified QDs with a variety of biological targeting moieties (e.g., small molecule [9], peptide [10, 11], aptamer [12]) allowed successful identification with high resolutions for tumor cells in vivo. Further recent studies for QDs for optical imaging have been particularly focused on improving the imaging sensitivity with use of near-infrared (NIR)-emitting QDs or decreasing the toxicity by using Cd-free QDs.

QDs that emit in the near-infrared (NIR) region (700–900 nm) can minimize the problems of endogenous fluorescence of tissues (autofluorescence) and increase tissue penetration, which is particularly suitable for in vivo animal imaging [14, 15]. In a pioneering study, Bawendi and coworkers first reported core/shell (CdTe/CdSe) QDs with fluorescence emission at 840–860 nm while preserving the absorption cross section (Fig. 2a, b) [13]. These NIR-emitting QDs were then rendered soluble and stable in serum by polydentate phosphine coating and used for to identify cancer cells in lymph nodes during surgery (sentinel lymph node mapping). As shown in Fig. 2c, when these QDs (10 pmol) were intradermally injected to the mouse, they entered the lymphatics and migrated within minutes to an axillary sentinel lymph node (SLN) that could be detected using intraoperative NIR fluorescence imaging system. Furthermore, even in a large animals (pigs), the authors found NIR fluorescence from intradermally injected ODs (400 pmol) was sensitive enough for imaging SLN 1 cm deep in real time and ensuring complete resection of the SLN under optical image guidance (Fig. 2d) [13].

Second near-infrared (NIR-II) window is nearly biologically transparent due to its much less optical scattering from endogenous molecules (e.g., hemoglobin, melanin, lipids), and thus NIR-II imaging can afford deeper anatomical penetration at high spatial resolution, compared to NIR-I imaging [17]. Hence, in 2010, the Dai group has developed single-walled carbon nanotubes (SWCNTs) as sensitive NIR-II fluorescent probes for whole-body imaging as well as real-time intravital small vessel imaging. Here, SWCNTs were emitted in the NIR-II region (1,000–1,400 nm) upon excitation by a 785 nm laser, with large Stokes shift up to ~400 nm (Fig. 3a) and thus allowed for high spatial (~30 mm) and temporal (<200 ms per frame) resolution for small-vessel imaging at 1–3 mm deep in the hind limb (Fig. 3b) [16]. Also, these NIR-II-emitting SWCNTs have permitted the high through-skull fluorescence imaging of mouse cerebral vasculature to a depth of >2 mm in mouse brain with sub-10-μm resolution [18]. However, the optical cross section of SWCNT is a bit limited, and thus Ag_2S QDs have been developed with 5.6 times higher photoluminescence quantum yield than SWCNT for emission in the NIR-II region. These probes also have negligible cytotoxicity [19] and the potential for deep tissue imaging (with theoretical penetration depth of 5 cm) [20]. Ag_2S QDs can be used to study angiogenesis mediated by a tiny tumor (2–3 mm in diameter) [21]. More recently, Bawendi and coworkers introduced InAs-based, core/shell QDs

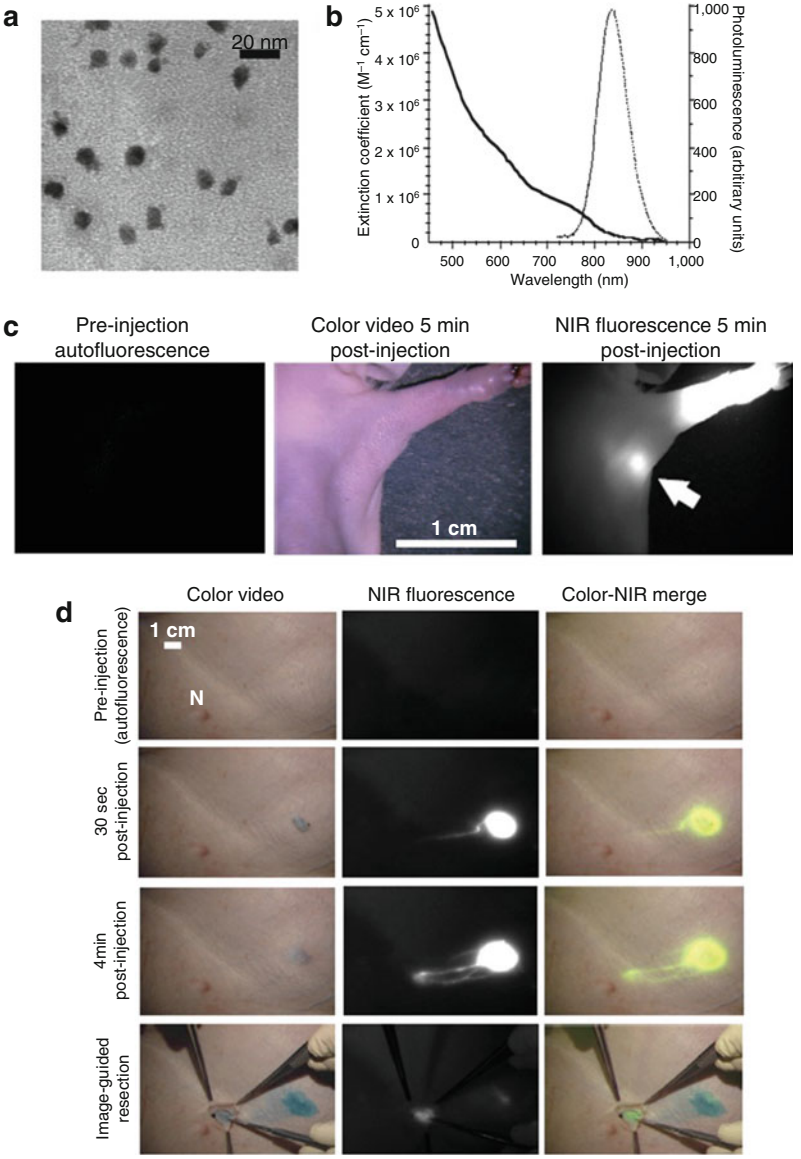

Fig. 2 NIR-emitting QDs for sentinel lymph node (SLN) mapping in the mouse and pigs. (**a**) TEM image of NIR QDs. (**b**) Molar extinction coefficient (solid curve) and photoluminescence intensity (dashed curve) of NIR QDs. (**c**) Images of mouse intradermally injected with NIR QDs (10 pmol) to the left paw; preinjection (autofluorescence), 5 min postinjection color video image, 5 min postinjection NIR fluorescence image. The putative axillary sentinel lymph node (SLN) is indicated by a white arrow. (**d**) Images of the surgical procedures in the pig intradermally injected with NIR QDs (400 pmol) at different time points; preinjection (autofluorescence), 30 s postinjection, 4 min postinjection, and during image-guided resection. Adapted from Kim et al. [13] with permission

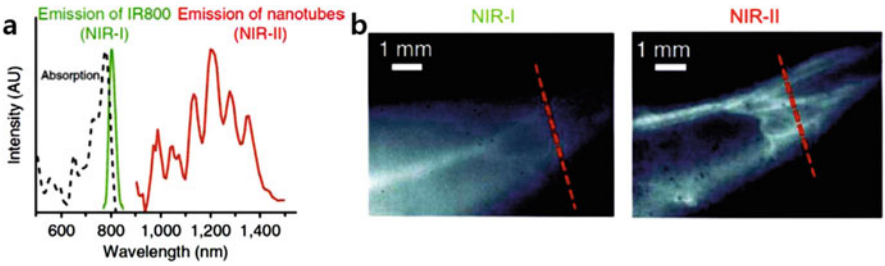

Fig. 3 In vivo mouse imaging in the NIR-II region. (**a**) The absorption spectrum of SWCNT-IRDye-800 conjugates (black dashed line), the emission spectrum of IRDye-800 dye (NIR-I) (green line), and SWCNTs (NIR-II) (red line). (**b**) NIR-I and NIR-II fluorescence images of a mouse injected with the SWCNT-IRDye-800 conjugates. This led to clearer vasculature imaging in the NIR-II region. Adapted from Hong et al. [16] with permission

(e.g., InAs/CdSe or InAs/CdSe/ZnSe) leading to a dramatically higher quantum yield (10 times to Ag_2Se QDs) and size-tunable emission in NIR-II region. In this study, they demonstrated that these QDs functionalized via three distinct surface coatings (e.g., triglyceride-rich lipoproteins, phospholipid micelles, PEG2000 PE) can allow for functional imaging to measure metabolic rates of lipoproteins in several organs and heartbeat/breathing rates as well as to quantify the blood flow of mouse brain vasculature [22].

Despite all of these photo-physical advantages of QDs, a substantial challenge for conventional Cd-containing QDs is their inherent cytotoxicity [23]. For example, CdSe QDs were found to induce cell death due to the liberated free Cd^{2+} from the CdSe lattice. Therefore, many studies have been performed to develop Cd-free QDs (e.g., InP, InAs, Ag) with comparable or even better performance than existing Cd-containing QDs [24]. Surface passivation via an additional inorganic shell (e.g., ZnS capping of CdSe QDs) is another way of reducing the oxidation-mediated cytotoxicity of Cd-QDs; here, PL improvement also appears owing to the effective passivation of surface non-radiative recombination of excitons [25]. Nevertheless, besides the aforementioned composition controls, toxicity issues can be circumvented by size control of QDs to make them renally clearable. In a pioneering study using QDs as a model inorganic nanoparticle, Frangioni and coworkers proposed the design considerations to reduce metal-induced toxicity [26]. In this study, it was revealed that nanoparticles of hydrodynamic diameter <5.5 nm could be efficiently excreted in urine via systemic intravenously injections.

3 Anti-Stokes Shift Luminescent Nanoparticles

Anti-Stokes shift luminescence is a special optical process of converting (low energy) long wavelength of light to (higher-energy) short-wavelength radiation, which can permit the deeper tissue penetration with minimal photo-bleaching

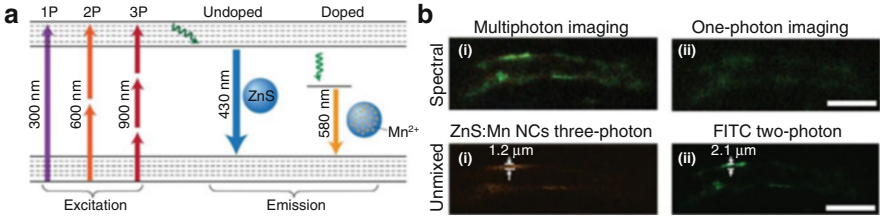

Fig. 4 Multiphoton fluorescence imaging with manganese-doped ZnS QDs (ZnS:Mn QDs). (**a**) A Jablonski diagram comparing one-, two-, and three-photon fluorescence of QDs. While the normal fluorescence emission from ZnS QDs is near 430 nm, ZnS:Mn QDs redshifts the emission to 580 nm reducing tissue absorbance and scattering of emitted light. Adapted from Zagorovsky et al. [28] with permission. (**b**) Comparison between a multiphoton micrograph (i) and a one-photon confocal laser-scanning micrograph (ii), which were acquired from spectral fluorescence of the tumor vasculature targeted by ZnS:Mn QDs-RGD-FITC conjugates (top). Comparison between three-photon luminescence of ZnS:Mn QDs (i) and two-photon luminescence of FITC (ii), which were acquired from spectral unmixing of the tumor vasculature targeted by ZnS:Mn QDs-RGD-FITC conjugates (bottom). Adapted from Yu et al. [29] with permission

[27]. Among the various anti-Stokes optical processes, both multiphoton absorption and upconversion mechanisms have been given much attention in recent years.

Transition metal-doped semiconductor nanoparticles can exhibit high multiphoton light absorption. In particular, three-photon imaging can effectively reduce the out-of-focus excitation and background autofluorescence; thus, in a recent study by Hyeon and coworkers, manganese-doped ZnS QDs (ZnS:Mn QDs) were developed to exhibit a large three-photon cross section ($1.3\ (\pm 0.5) \times 10^{-79}$ $cm^6\ s^2\ photon^{-2}$) [29]. Interestingly, in this study, manganese doping redshifted the emission wavelength of ZnS QDs from 430 to 580 nm to attain more efficient light path through tissue (Fig. 4a). Therefore, upon NIR excitation with a deep-penetrating 920 nm laser, three-photon optical imaging with ZnS:Mn QDs exhibited better resolution compared to two-photon imaging with fluorescein isothiocyanate (FITC) (Fig. 4b). This also allowed highly resolved imaging of tumor vasculatures with an experimental penetration depth of ~3 mm [29]. These QDs also have a large two-photon absorption cross section under irradiation of NIR-II light (1,050–1,310 nm) and improved the penetration depth and imaging quality [30].

Lanthanide ion-doped nanoparticles are a new generation of luminescent probes to achieve photon upconversion. Typical upconversion nanoparticles (UCNPs) consist of Yb^{3+} ion as a sensitizer and Er^{3+} ion as an emitter to generate the visible green emission upon excitation at 980 nm [33, 34]. Similar to ZnS:Mn QDs, NIR light absorbing, UCNPs can allow the imaging of deeper tissue penetration than conventional QDs (Fig. 5a) [31]. In addition, UCNPs can be used for multicolor multiplexed imaging [32] because they can exhibit tunable emission (blue, green, to red) by varying the lanthanide dopant ions (Fig. 5b) [35, 36]. The UCNPs offer sequential photon absorption via real intermediate, long-lived, electronic states of dopant ions, while the metal-doped semiconductors have multiphoton absorption based on virtual intermediate states [37, 38]. Consequently, UCNPs do not need

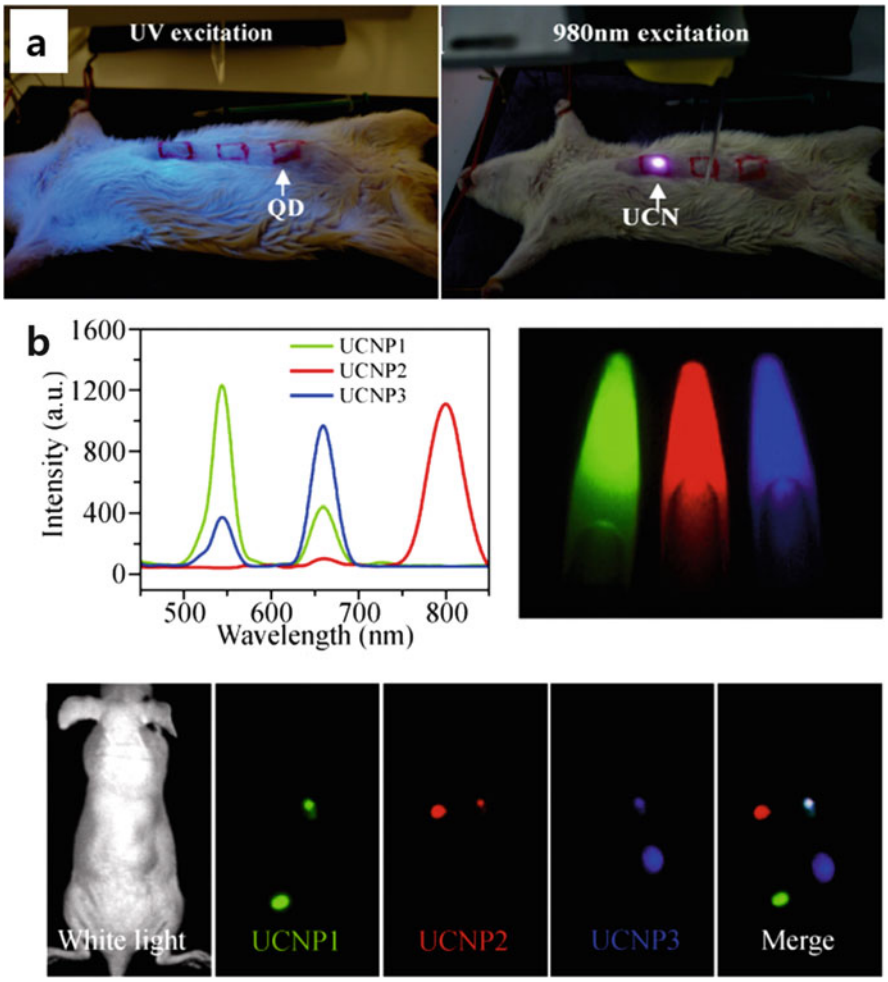

Fig. 5 (**a**) In vivo imaging of rat subcutaneously injected to abdominal skin with green-emitting QDs (CdTe) under UV excitation (left) and green-emitting UCNPs of PEI/$NaYF_4$:Yb,Er under NIR excitation (right). Adapted from Chatterjee et al. [31] with permission. (**b**) Multicolor imaging of a mouse using NIR-to-blue UCNPs of $NaY_{0.78}Yb_{0.2}Tm_{0.02}F_4$, NIR-to-green UCNPs of $NaY_{0.78}Yb_{0.2}Er_{0.02}F_4$, and NIR-to-red UCNPs of $NaY_{0.78}Yb_{0.3}Er_{0.01}F_4$: three colors of UCNPs were clearly differentiated after spectral unmixing. Adapted from Cheng et al. with permission [32]

expensive high-power, femtosecond pulsed laser [39] and can be excited by continuous-wave (CW) diode lasers operating at low power (1 W cm^{-2}) [40] – this can facilitate fast imaging using a wide-field microscopy. In summary, NIR light-absorbing, real-time imaging UCNPs offer broad applications as real-time, long-term tracker for cell imaging [41] as well as sensitive contrast agent with high-contrast resolutions for whole-body optical imaging [42].

However, one limitation for the conventional Yb^{3+}-doped UCNPs [42] is the heating effect that is generated by water molecules under 980 nm laser excitation. Therefore, in recent years, considerable effort has been made to control the excitation wavelength because this is where water has lower absorption. In one study, Andersson-Engels and coworkers utilized $NaYbF_4$:Tm;Er and $NaYbF_4$:Tm;Ho nanoparticles under 915 nm excitation [43]. Nd^{3+} was introduced to the conventional Yb^{3+}-doped UCNPs as a new sensitizer to be excited at 800 nm [44]. These nanoparticles showed a larger absorption cross section and deeper image penetration depth than those with 980 nm excitation. It is also very desirable to construct UCNPs with both excitation and emission in the NIR range (NIR_{in}-NIR_{out} UCNPs) to further improve the imaging contrast. Therefore, Prasad and coworkers reported core/shell (α-$NaYbF_4$:Tm^{3+})/CaF_2 nanoparticles with excitation at ~980 nm and PL emission at 800 nm. In this study, the authors found that these nanoparticles allowed tenfold higher signal-to-background ratio (SBR) than previously reported UCNPs for in vivo imaging enabling deep-penetration imaging through 3.2 cm pork tissue [45].

4 Carbon Dots, Porous Silicon Nanoparticles, and Au Nanoclusters

Quantum-sized carbon- and silicon-based optical imaging probes have recently been developed as benign alternatives to conventional semiconductor QDs. Although these nanomaterials lack a classical bandgap structures of QDs, they can achieve fluorescence emission from the surface passivation-created defects (surface energy traps [46]). Here, surface passivation stabilize the surface defects and facilitate more effective radiative recombination of surface-confined excitons [47, 48].

In a pioneering study, Sun et al. [49] prepared 5 nm carbon dots (C-Dots) via laser ablation of graphite powder and cement. The surface of the C-Dots was then effectively passivated with organic moieties (diamine-terminated oligomeric PEG; PEG1500N) resulting in strong photoluminescence with no blinking as well as tunable emissions from visible to NIR under the argon ion laser excitation (458 nm) [49]. They also found that these C-Dots capped with poly-(propionylethylenimine-co-ethylenimine) (PEI-EI) were two-photon active with pulsed laser excitation in the NIR region (800 nm). The two-photon absorption cross sections of the C-Dots were comparable with the best-performing semiconductor QDs. Next, upon incubation to the human breast cancer cells, the authors demonstrated the potential of C-Dots for cell imaging with two-photon luminescence microscopy [50]. Indeed, recent studies have included the careful selection of carbon source as well as surface modifier for C-dots with enhanced photoluminescence [51] resulting in C-Dots with a quantum yield 2–2.5-fold that of CdSe/ZnS QDs [52, 53]. In particular, C-dots can offer significant advantages in terms of potential translatability and applicability because they exhibit very low toxicity and great availability in scale-up production through various inexpensive renewable resources [54–56].

Quantum-sized, porous silicon nanoparticles prepared by electrochemical etching of silicon wafer have subsequent luminescence arising in the 600–1,000 nm range from a combination of a quantum confinement effect and surface defect localized at the Si-SiO_2 interface [59]. Porous silicon has become one of the most powerful nanomaterials for optical in vivo imaging with respect to its adaptability, biodegradability, and capability for background-free imaging. Porous silicon nanoparticles are highly adaptable to load large volumes of various drugs (e.g., small molecules, nucleic acid, protein drugs) or additional imaging agents (e.g., Gd complex, magnetic particles) within their size-tunable pores [60]. Porous silicon nanoparticles can biodegrade into benign orthosilicic acid ($Si(OH)_4$; the element silicon itself is an endogenous substance (Fig. 6a) followed by excretion as urine [57]. The intravenously administered porous silicon nanoparticles were completely degraded in 4 weeks without any measurable in vivo toxicity over 1–12 months (Fig. 6b, c). In addition, porous silicon nanoparticles enable autofluorescence-free and time-gated fluorescence (TGF) imaging of tissue in vivo because they can provide the unusual long emission lifetime (5–13 ms) compared to nanosecond lifetimes of typical fluorescent organic molecules or QDs [58]. Thus, in time-gated fluorescence (TGF) imaging (images are captured at a delayed time after excitation), the signal could be effectively eliminated from the shorter-lived emission signals.

Figure 6d shows a nude mouse injected subcutaneously with PEGylated luminescent porous silicon nanoparticles (PEG-LPSiNPs). Here, the TGF imaging revealed intensive signals in the PEG-LPSiNP injection (T1) with negligible signals from the Cy3.5 injection (T2) or from the background tissue autofluorescence (T3). The fluorescent signals appeared in all three spots under the continuous-wave (CW) imaging (steady-state conditions; no time gating). Therefore, as an alternative to cytotoxic QDs, there has been much progress in the use of porous silicon nanoparticles for multimodal bio-imaging [61] and targeted therapy [62]. However, considerable future research still remains to overcome the limitations of luminescent porous silicon nanoparticles such as low quantum yield and difficulty in size-controlled mass production.

Gold nanoparticles (10–100 nm in size) are an efficient light scattering and absorbing center known to generate visible luminescence and heat upon excitation at λ_{SPR} based on its surface resonant oscillation of electrons [63]. In contrast, gold nanoclusters (AuNCs) consisting of several tens of atoms (<2 nm in size) have molecular-like, discrete electronic states due to the spatial confinement of free electrons [64]. Therefore, gold nanoclusters can feature all unique optical properties that semiconductor QDs have. In the past decade, there have been many investigations of synthetic methods for fine control of the number of gold atoms in a cluster.

Generally, gold nanoclusters (AuNCs) are synthesized by the chemical reduction of gold precursors in the presence of strong stabilizer. Owing to a strong affinity of thiols to the Au surface, thiol-containing small molecules (e.g., glutathione [66, 67], dodecanethiol [68]) have been extensively used as a stabilizing template for gold clusters [69]. As a simple, green synthetic route, macromolecules (e.g., protein [70], DNA [71], dendrimer [64]) have also been also employed as a surface template to direct the formation of Au clusters with a substantial quantum yield (e.g., bovine

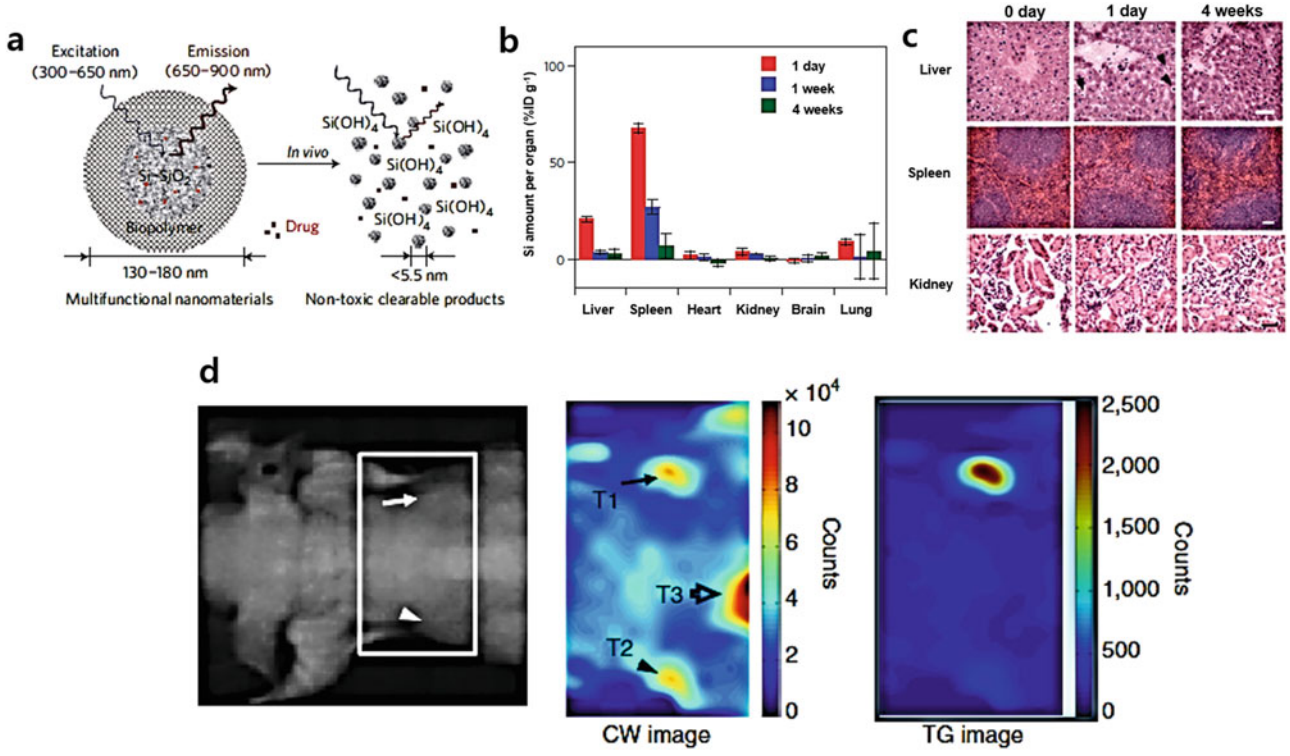

Fig. 6 (**a**) Schematic illustrations describing the structure and in vivo biodegradation process of luminescent porous silicon nanoparticles (LPSiNPs). (**b**) Biodistribution and biodegradation of LPSiNPs for 1 month in the mouse with intravenously injection of LPSiNPs (20 mg/kg). (**c**) Histopathological analysis of the tissue sections from the organs (kidneys, liver, and spleen) in the mouse with LPSiNPs. Adapted from Park et al. [57] with permission. (**d**) Continuous-wave (CW) and time-gated fluorescence (TGF) imaging of LPSiNPs from the mouse with subcutaneous injection of LPSiNPs; PEG-LPSiNP injection (T1), Cy3.5 injection (T2), and background tissue autofluorescence (T3). Adapted from Gu et al. [58] with permission

serum albumin (BSA)-protected Au_{25}: ~6% QY). In particular, Jin and coworkers reported that surface ligands with many electron-rich atoms (e.g., N, O) or groups (e.g., –COOH, NH_2) can promote the fluorescence of gold clusters either by charge transfer through the Au-S bonds or by direct donation of delocalized electrons to the metal core [72].

Besides the aforementioned route ("Au atoms to Au clusters"), there is alternative route to prepare gold nanoclusters by etching the surface atoms of gold nanoparticles by appropriate ligands. For example, gold nanoclusters capped with dihydrolipoic acid (AuNC@DHLA) with a quantum yield of around 1–3% were synthesized. Upon etching and ligand exchanging with DHLA, the original gold nanoparticles stabilized with didodecyldimethylammonium bromide (AuNP@DDAB) (~5.6 nm) becoming smaller. These water-soluble gold clusters (<2 nm) have red photoluminescence under UV excitation (Fig. 7) [65]. As for the etchant, hyperbranched polymers were also applied to induce the gold nanoclusters with a quantum yield of 10–20% [73].

The photoluminescence quantum yield of gold clusters is still lower than the organic fluorophore or QDs. However, they are ultra-small and exceptionally biocompatible nanoparticles with reduced photo-blinking behavior. Therefore, in a recent study by Hung-I Yeh and coworkers, gold nanoclusters have been exploited as a fluorescent biomarker for live cell tracking in vivo using hind-limb ischemic mice. Here, the Au clusters showed nonspecific incorporation into living endothelial progenitor cells (EPC) with no acute cytotoxicity. Thus, after intramuscular injection of Au-labelled human EPC, the cells preserved angiogenic potentials and exhibited detectable fluorescent signals for up to 21 days [74].

In another example to demonstrate utility in the early diagnosis for cancers, mice with MDA-MB-45 and HeLa tumor xenografts were treated with ultra-small NIR-emitting Au nanoclusters (BSA-capped gold cluster). These clusters accumulated in the tumors and showed tumor-to-background signals of ~15 for 6 h postinjection [75]. Most importantly, gold nanocluster can also have good clearance after administration through the kidneys due to its renal cutoff size (<5.5 nm) (this is below the kidney filtration threshold (7–8 nm). Zheng et al. recently demonstrated renal-clearable, NIR-emitting, gold nanoclusters (zwitterionic thiolated gold clusters) enabling the real-time fluorescence visualization of kidney clearance kinetics with a 50-fold increase of contrast to conventional organic dyes. This is a useful and sensitive tool for early staging of kidney dysfunctions [76].

5 Nano-diamond and Persistent Luminescent Nanoparticles

Nano-diamonds (ND) mainly consist of sp^3 carbon and are optically transparent, biologically inert, and chemically modifiable. When these materials are irradiated by high-energy ion beam, followed by thermal annealing, they can be immobilized with a high concentration of point defects (e.g., nitrogen-vacancy (NV^-) complexes) in the sp^3 carbon lattice (Fig. 8a) [77]. These point defects can form a photoluminescent

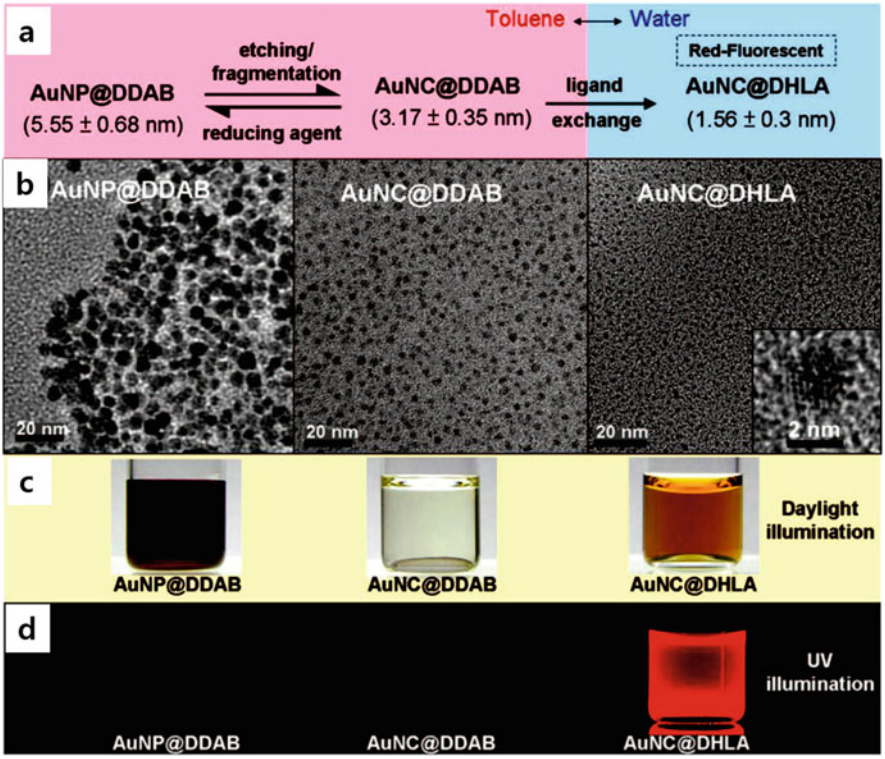

Fig. 7 Strategy to synthesize water-soluble fluorescent Au nanoclusters (AuNC) via ligand-assisted etching of gold nanoparticles (AuNP). (**a**, **b**) Gold nanoparticles stabilized with didodecyldimethylammonium bromide (AuNP@DDAB) (5.6 nm) are etched by the addition of Au precursors ($HAuCl_4$ or $AuCl_3$) to smaller nanoclusters (AuNC@DDAB) (3.2 nm). They become water-soluble upon ligand exchange with dihydrolipoic acid (DHLA). (**c**, **d**) Only the AuNC@DHLA solution (<2 nm) shows the red photoluminescence under UV excitation. Adapted from Lin et al. [65] with permission

center to produce a broad light absorption at 550 nm and emission at 700 nm. There are many unique optical properties that are not shown in conventional florescence dyes. This fluorescent nanoparticle is exceptionally photostable with no photo-bleaching under continuous high intensity of light excitation [78, 79]. The fluorescence lifetime is much longer (five- to sevenfold) than that of biological tissue, which can facilitate background, autofluorescence-free imaging (Fig. 8b) [80]. Therefore, nano-diamonds have been extensively exploited as cellular biomarkers for long-term in vitro and in vivo imaging applications [81].

Nano-diamonds can be used with super-resolution microscopy to track single molecules or image subcellular structures on the nanometer scale. In a pioneering study, stimulated emission depletion (STED) microscopy was used to overcome the diffraction limit of light: Chang et al. showed that single fluorescent nano-diamond (30 nm BSA coated nano-diamonds) can be distinguished in cells with a sub-diffraction spatial resolution of approximately 40 nm [83]. Typical confocal

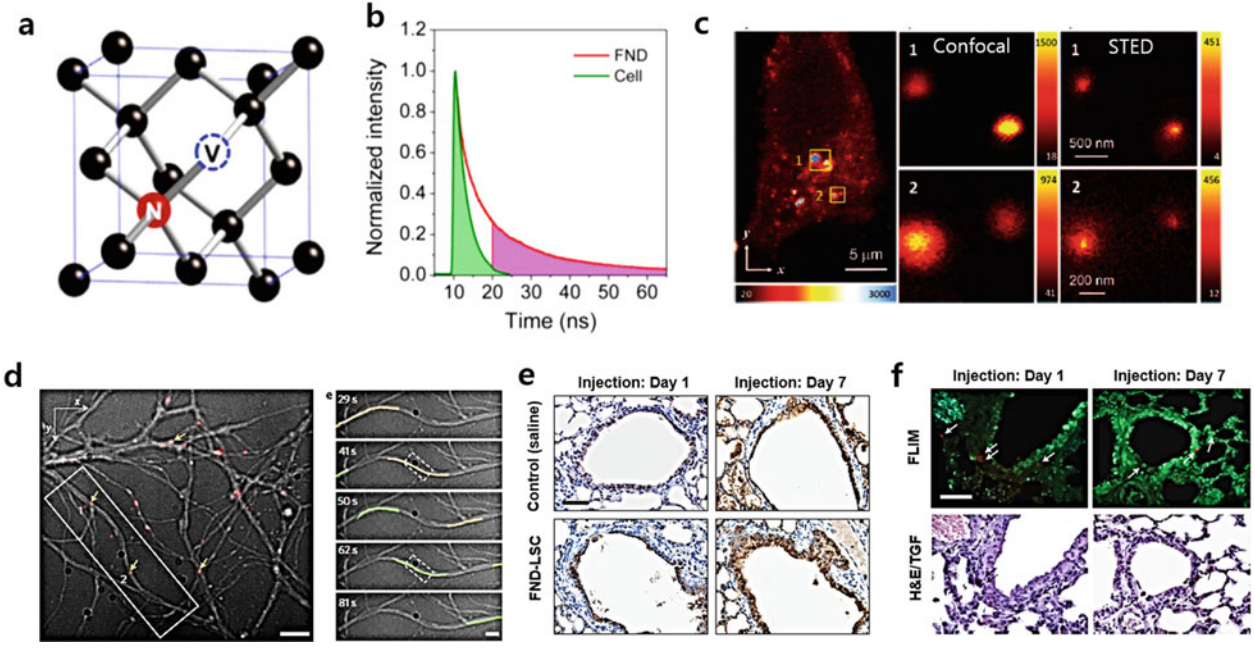

Fig. 8 (**a**) Structure of fluorescent nano-diamond (ND). (**b**) Comparison between the fluorescence lifetimes of NDs in water (red) and endogenous fluorophores in cells (green). The background-free detection can be facilitated by time-gated imaging at 10 ns. Adapted from Hsiao et al. [82] with permission. (**c**) Confocal and STED imaging of HeLa cells labelled with BSA-conjugated NDs by electroporation. Adapted from Tzeng et al. [83] with permission. (**d**) Intraneuronal transport monitoring by ND tracking assay. Bright-field (BF) images of the neuronal branches were merged with the fluorescence (FL) channel images, showing the movement of NDs within dendrites (yellow arrows). More specifically, the two ND-containing endosomes moved toward the cell soma (labelled 1 and 2 on left images). The movement of two NDs was also determined by particle tracking (1 in yellow; 2 in green) with a persistence of 10 s at different time points (right images). Adapted from Haziza et al. [84] with permission. (**e**, **f**) ND-labelled lung stem cells (LSCs) in lung-injured mice. (**e**) Immunostaining analysis indicated that the bronchiolar epithelium of the mice injected with ND-labelled LSCs was observed with repopulation of $CCSP^{+}$ cells (brown) at day 7. These materials had a higher regenerative capacity with rapid restoration of lung epithelium. (**f**) Representative fluorescence lifetime imaging microscopy (FLIM; top) and TGF/H&E staining images (bottom) from the same lung tissue sections show that ND-labelled LSCs (white and black arrows, respectively) were located to the terminal bronchioles of the lungs. Adapted from Wu et al. [85] with permission

microscopy cannot resolve whether the particles are internalized or well-dispersed/aggregated due to the diffraction-limited image resolutions; however, STED microscopy images successfully identified the individual nano-diamond in the cytoplasm (Fig. 8c). This not only identifies the cellular process, but the nano-diamonds (ND) can also provide further information on cellular function in disease diagnostics.

For example, a ND-based tracking assay was recently developed to observe intraneuronal transport abnormalities with a spatial resolution of 12 nm and a temporal resolution of 50 ms. [84] Figure 8d shows that when NDs were internalized to primary hippocampal neuron cells, they could be tracked in real time using pseudo-total internal reflection fluorescence video microscopy (pseudo-TIRF). Here, the overlay images (BF and FL) can display the precise localization of ND overall trajectories and movement throughout the microtubules. Therefore, using the primary hippocampal neurons treated with amyloid-β_{1-42} peptide, the authors successfully found the decreased transport velocities of ND – this indicates abnormal intraneuronal transport in Alzheimer's disease.

In addition, exceptionally biocompatible and photostable, fluorescent nano-diamonds (NDs) can allow the monitoring of the long-term fate of stem cells in vivo. In a recent study, Wu et al. delivered ND-labelled lung stem cells (LSCs) by intravenous injection and observed their engraftment and regenerative capabilities with single-cell resolution through time-gated fluorescence (TGF) imaging and immunostaining [85]. Here, the authors first demonstrated that fluorescent nano-diamond labelling did not impair the lung stem cells' self-renewal and differentiation into type I and type II pneumocytes. Since the regenerative capacity of LSCs could be activated after tissue injury, using naphthalene-injured mice, they found that the transplanted LSCs migrated and integrated into bronchiolar epithelium of the murine lungs to successfully regenerate the damaged epithelial linings (Fig. 8e, f). However, this still required a sufficiently large number of photoluminescent nitrogen-vacancy (NV) centers to increase the optical cross sections for fluorescent nano-diamonds. Unfortunately, the use of nano-diamonds is still limited in multiplexed imaging.

Persistent luminescent nanoparticles store energy by pre-charging with UV excitations and gradually releasing the photon energies. The emission is steady for several hours or days with no additional input of energies. Therefore, there is no need for external continuous excitation – this approach can lead to sensitive imaging without background autofluorescence [86]. Scherman and coworkers prepared silicate crystals doped with Eu^{2+}, Dy^{3+}, and Mn^{2+} ions via a sol-gel process followed by successive high temperature calcination. These nanoparticles possess energy traps where the excited lights can be non-radiatively captured to induce persistent luminescence. They found that these particles can successfully emit light at 700 nm with a long-lasting luminescence for more than 1 h upon excitation ex vivo by UV light (6 W UV lamp, $<$5 min). The authors have also shown that when such particles were pre-excited and implanted to BALB/c mice, the sensitive fluorescent signals could be easily detected in real time using a photon counting system [87]. However, these probes could only be excited ex vivo by UV lights, which prevent long-term imaging in vivo.

One possible strategy is to develop a new class of nanoparticles whose persistent luminescence can be renewable in vivo through living tissues. In 2014, Scherman and coworkers synthesized 80 nm Cr^{3+}-doped zinc gallium oxide (ZGO) nanoparticles and observed whether the persistent luminescence can be activated in situ whenever required with no time limit [88]. The particles have several excitation peaks with one within the tissue transparency window (rectangle with hatching) (Fig. 9a) resulting in a NIR = persistent luminescence by a low-powered, orange/red light-emitting diode (LED) illumination (Fig. 9b). Simple illumination through living tissues with visible light was sufficient to activate persistent luminescence of ZGO-OH nanoparticles – intense signals were shown from the reticuloendothelial system (RES) organs (e.g., liver) within the deep tissues (Fig. 9c). As for the applications, the authors assessed the ability of as-prepared nanoparticles for in vivo imaging for vasculature imaging, tumor detection, and longitudinal cell tracking in a mouse model. With additional surface coating (amino, carboxy, or PEG), these nanoparticles become very colloidal stable and long circulating after intravenous injections; therefore, they successfully showed these persistent luminescent nanoparticles could be used to image the tumors via passive targeting (PEG coating) (Fig. 9d). Furthermore, the amino-coated probes could label macrophage cells for visualization in vivo (Fig. 9e). Additionally, the pathway of nanoparticles could be detected in the gastrointestinal tract after oral administration.

6 Dye-Doped Inorganic Nanoparticles (Calcium Phosphate, Silica)

Biologically resorbable and optically transparent inorganic materials (e.g., calcium phosphate, silica) can encapsulate dyes into their well-defined, large-surfaced, nanoporous structures and are an effective way of enhancing the photostability of organic fluorophores. These dye-doped nanoparticles can minimize their fluorescence quenching or enzymatic degradation. However, to achieve high sensitivity and specificity of the fluorescence signals, it is critically important to select appropriate dye molecules and increase the loading capacity with no change in particle size and morphology.

Calcium phosphate is found in endogenous biominerals including bone and teeth. It can easily form colloidally stable nanoparticles by reverse microemulsion synthesis [90]. In the first such study, Adir et al. successfully synthesized and investigated the potentials of NIR-emitting calcium phosphate nanoparticles (CPNPs) by entrapping indocyanine green (ICG) [91]. In this study, they prepared the well-dispersed, ICG dye-doped CPNP (ICG-CPNP) (Fig. 10a), and found that the photostability is 500% longer relative to the free dye (Fig. 10b). PEGylated ICG dye-doped CPNPs exhibited much longer blood circulation than free ICG (free ICG in physiological environments experience the rapid aggregation and clearance from the body) and passively accumulated to xenografted breast

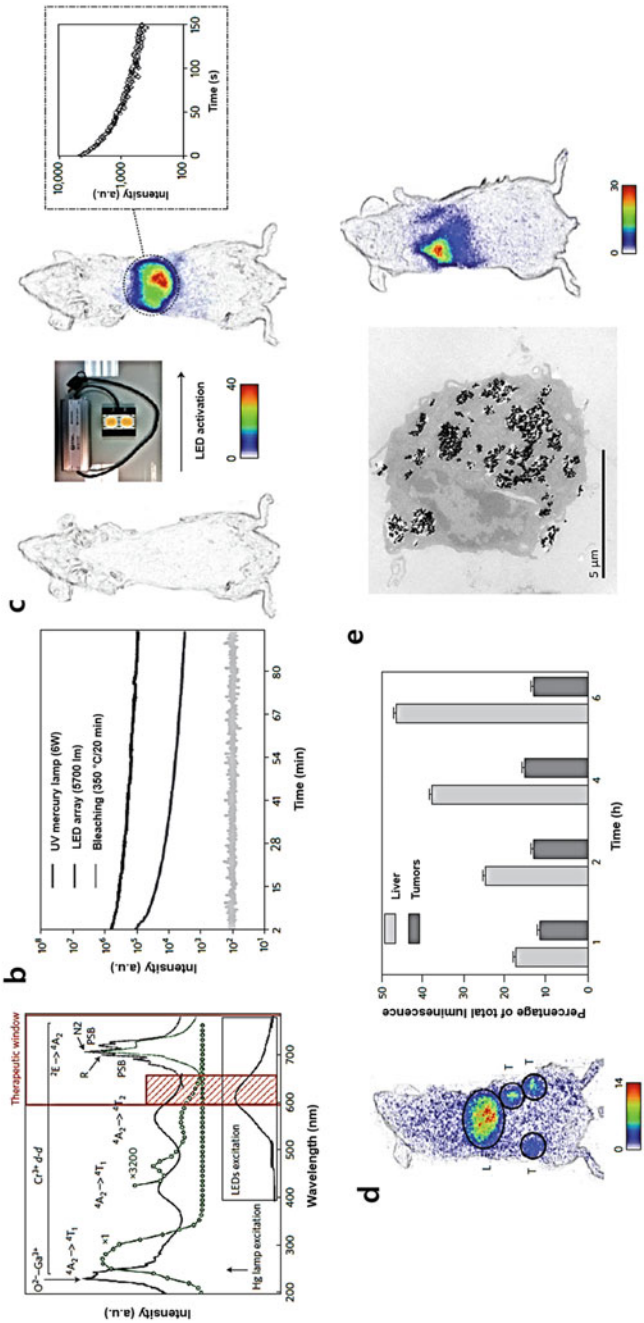

Fig. 9 (**a**) PL excitation (black line) and emission (red line) spectra of Cr^{3+}-doped zinc gallium oxide (ZGO). (**b**) Persistent luminescence decay curves from Cr^{3+}-doped ZGO obtained at 2 min excitations either by UV light or LED array source. (**c**) The detection of persistent luminescence nanoparticles after in vivo activation. Here, the animals intravenously injected with ZGO-OH were irradiated with an orange/red LED source for 2 min, and images were acquired for 3 min with the photon counting system. The inset shows a persistent luminescence decay curve from the liver. (**d**) The biodistribution of persistent luminescence nanoparticles in a tumor-bearing mouse. Images were acquired 4 h after the injection of ZGO-PEG nanoparticles following visible activation of persistent luminescence with orange/red LED illuminations, which clearly showed the enhanced tumor uptakes as well as the accumulation kinetics. (**e**) ZGO-NH_2 persistent luminescence NPs used for labelling of RAW cells in vitro (left images) and cells tracking in vivo (right images). Adapted from Maldiney et al. [88] with permission

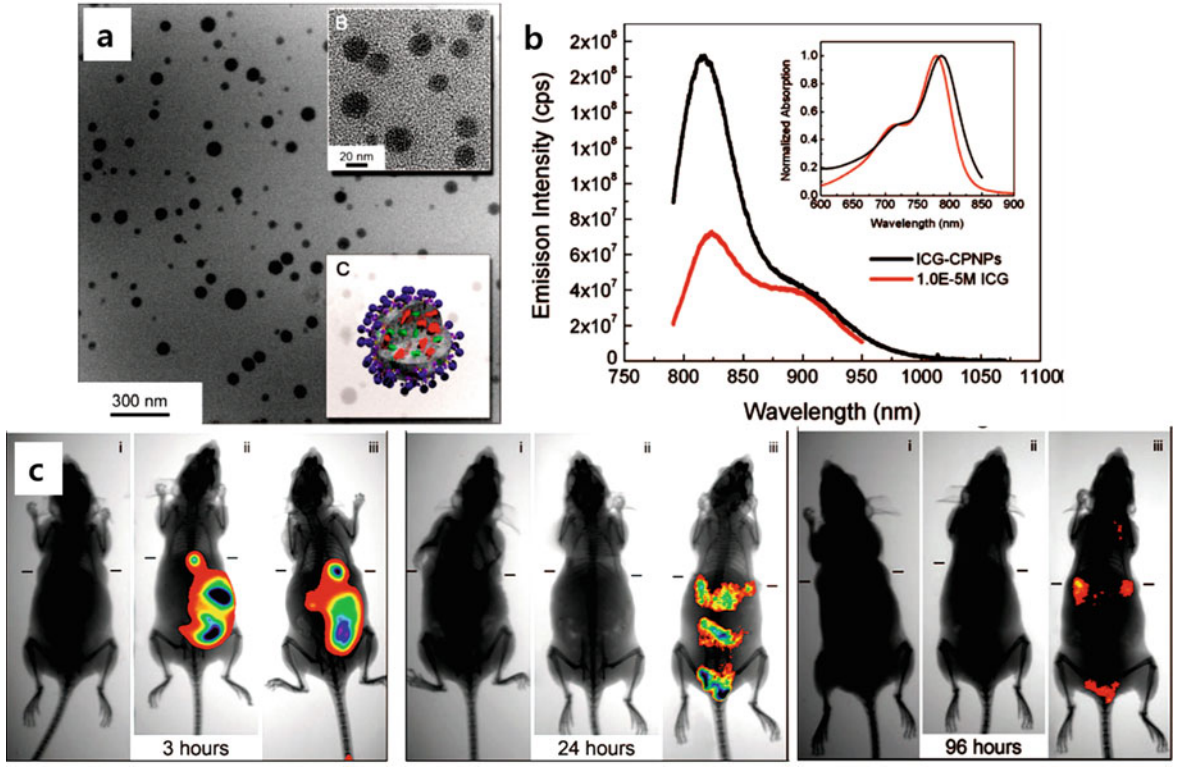

Fig. 10 (**a**) TEM images and schematics of ICG dye-encapsulating calcium phosphate nanoparticles (ICG-CPNP). (**b**) Fluorescence emission spectra of free ICG (red) and ICG-CPNPs (black). The inset displays the absorption spectra. (**c**) NIR images (Ex. 755 nm, Em. 830 nm) acquired at various time points (3, 24, and 96 h) to track the fluorescence signals from the carboxylate-terminated CPNPs without ICG (i), free ICG (ii), and PEGylated ICG-CPNPs (iii). Nanoparticles were systematically delivered via tail vein injections to nude mice bearing human breast adenocarcinoma tumors. No fluorescence signal was detected from the free ICG (ii) at 24 h postinjection, while the PEG-ICG-CPNP sample (iii) exhibited significant fluorescent signal even after 96 h postinjection. Adapted from Altinoglu et al. [89] with permission

adenocarcinoma – the fluorescence signals lasted >96 h post-systemic injection (Fig. 10c) [89]. In the next study, they further modified these nanoparticles with active targeting moieties of human holotransferrin, anti-CD71 antibody, and short gastrin peptides. They validated the systemic in vivo targeting to breast and pancreatic cancer lesions, respectively [92].

Elemental silicon itself is an endogenous substance, and it has been used extensively to fabricate (porous) silica nanostructures with a well-defined size and morphology via simple sol-gel synthesis [61]. Fluorescent dye molecules can be physically entrapped into the porous nano-channels of silica matrix [93]. The fluorescence remained unquenched up to very high concentrations of dye molecules. In 2011, Igor Sokolov and coworkers described small silica particles (ranging from 20 to 50 nm) with a high dye loading capacity (0.8–9.3 mg rhodamin6G (R6G dye) per g particles) using several organotriethoxysilanes (MTMS, ETES, or PTES) for the co-precursors of silica. They found the relative brightness from the fluorescent dye-doped silica particles has 30–770 times a QY that is higher than non-dimerized R6G dye molecules and 1.5–39 times of CdSe/ZnS QDs [94]. Importantly, some fluorescent silica nanoparticles (e.g., Cornell dots; core-shell type of dye-rich core surrounded by denser silica network [95]) have exceptional biocompatibility and were approved for the first human clinical trials for cancer diagnosis [96]. These 6–7-nm-sized Cornell dots (containing the dye, Cy5) attached with cyclic arginine-glycine-aspartic acid (cRGDY) peptides that target integrin $\alpha_v\beta_3$ and ^{124}I radiotracer for positron emission tomography (PET) imaging have been administered to five patients with metastatic melanoma [97]. Their favorable PK/biodistribution profiles and safety assessment showed the potential for clinical translation of these cancer-targeted, renally excreted inorganic nanoparticles. In addition to the visible light dyes (R6G, Cy5, FITC), NIR-emitting ICG dyes have also been encapsulated to the nanostructures of dense silica [98], mesoporous silica [99, 100], and porous silicon [101] and successfully utilized as for NIR optical imaging as well as for photoacoustic imaging in recent years.

7 Conclusion

Innovative nanotechnology has enabled the development of several new inorganic fluorescent nanomaterials to realize sensitive, high-resolution, optical imaging. QDs have been extensively investigated to overcome the limitations of organic fluorescent dyes with its superior photo-physical properties such as size-tunable photoluminescence, narrow emission, and low photo-bleaching. Chemical modifications with additional organic layers (e.g., PEG, targeting ligands) on QD surfaces can improve the blood circulation and diffusion of QD for sentinel lymph node (SLN) mapping, vasculature imaging, or more complex targeted imaging of tumor cells in vivo. Subsequently, further research has focused more on NIR-emitting QDs (NIR-I or NIR-II) (e.g., core/shell CdSe/CdTe QDs, Ag_2S QDs) to improve the imaging sensitivity of the conventional, visible luminescent QDs.

Based on the anti-Stokes shift luminescence mechanism and NIR light absorption, transition metal-doped semiconductor nanoparticles and lanthanide ion-doped nanoparticles (upconversion nanoparticles) offer high-resolution whole-body imaging with deep tissue penetrations (up to several ~cm). Interestingly, persistent luminescent nanoparticles were found to be excited (either by ex vivo or in situ) with no input energy during in vivo imaging resulting in minimal tissue autofluorescence. Nano-diamonds can also facilitate background-free imaging by time gating due to the longer emission lifetime than that of biological tissue. Additionally, some optically transparent inorganic nanomaterials (e.g., calcium phosphate, silica) have been used as a host matrix to encapsulate organic fluorophores to improve their physiological stability for longer in vivo imaging despite the fact they do not possess the intrinsic luminescence.

However, despite all of these considerable advances in inorganic fluorescent nanomaterials, there are still several challenging issues that need to be resolved. The unique optical properties of inorganic nanomaterials are generally dependent on their size, shape, and compositions, and thus large-scale synthesis is needed to maintain the uniformity of the nanoparticles between batches. In addition, due to the metal-induced toxicity, the potential safety issues of inorganic nanoparticles should be addressed for further clinical trials. An effective strategy is to make nanomaterials biodegradable into nontoxic byproducts (e.g., porous silicon nanoparticles) or nanomaterials that are solely composed of benign elements (e.g., silicon, silver, gold, calcium phosphate, carbon analogue) to exert less systemic toxicities. Renal clearance through urine can minimize the exposure of body to nanomaterials; likewise Au nanoclusters (<2 nm) or QDs with renal cutoff size (<5.5 nm) were found to be easily filtered by the kidneys. However, these changes can lead to trade-offs for the intended applications, and it is critical to tailor nanomaterials to balance between safety concerns, scale-up synthesis, and sensitivity/resolution that needs to fulfill the specific medical goal.

Compliance with Ethical Standards

Funding: This work was supported by the NIH R00 117048 and HL 137187.

Conflict of Interest: The authors declare that they have no conflicts of interest.

Ethical approval: This chapter does not contain any studies with human participants or animals performed by any of the authors.

References

1. Alivisatos AP (1996) Semiconductor clusters, nanocrystals, and quantum dots. Science 271:933–937
2. Jaiswal JK, Mattoussi H, Mauro JM, Simon SM (2003) Long-term multiple color imaging of live cells using quantum dot bioconjugates. Nat Biotechnol 21:47–51
3. Bruchez M, Moronne M, Gin P, Weiss S, Alivisatos AP (1998) Semiconductor nanocrystals as fluorescent biological labels. Science 281:2013–2016

4. Smith AM, Dave S, Nie SM, True L, Gao XH (2006) Multicolor quantum dots for molecular diagnostics of cancer. Expert Rev Mol Diagn 6:231–244
5. Gao X, Cui Y, Levenson RM, Chung LW, Nie S (2004) In vivo cancer targeting and imaging with semiconductor quantum dots. Nat Biotechnol 22:969–976
6. Maeda H, Wu J, Sawa T, Matsumura Y, Hori K (2000) Tumor vascular permeability and the EPR effect in macromolecular therapeutics: a review. J Control Release 65:271–284
7. Iyer AK, Khaled G, Fang J, Maeda H (2006) Exploiting the enhanced permeability and retention effect for tumor targeting. Drug Discov Today 11:812–818
8. Ruoslahti E, Bhatia SN, Sailor MJ (2010) Targeting of drugs and nanoparticles to tumors. J Cell Biol 188:759–768
9. Duman FD, Erkisa M, Khodadust R, Ari F, Ulukaya E, Acar HY (2017) Folic acid-conjugated cationic Ag2S quantum dots for optical imaging and selective doxorubicin delivery to HeLa cells. Nanomedicine 12:2319–2333
10. Gao J, Chen K, Luong R, Bouley DM, Mao H, Qiao T, Gambhir SS, Cheng Z (2012) A novel clinically translatable fluorescent nanoparticle for targeted molecular imaging of tumors in living subjects. Nano Lett 12:281–286
11. Cai WB, Shin DW, Chen K, Gheysens O, Cao QZ, Wang SX, Gambhir SS, Chen XY (2006) Peptide-labeled near-infrared quantum dots for imaging tumor vasculature in living subjects. Nano Lett 6:669–676
12. Jokerst JV, Raamanathan A, Christodoulides N, Floriano PN, Pollard AA, Simmons GW, Wong J, Gage C, Furmaga WB, Redding SW, McDevitt JT (2009) Nano-bio-chips for high performance multiplexed protein detection: determinations of cancer biomarkers in serum and saliva using quantum dot bioconjugate labels. Biosens Bioelectron 24:3622–3629
13. Kim S, Lim YT, Soltesz EG, De Grand AM, Lee J, Nakayama A, Parker JA, Mihaljevic T, Laurence RG, Dor DM, Cohn LH, Bawendi MG, Frangioni JV (2004) Near-infrared fluorescent type II quantum dots for sentinel lymph node mapping. Nat Biotechnol 22:93–97
14. Hilderbrand SA, Weissleder R (2010) Near-infrared fluorescence: application to in vivo molecular imaging. Curr Opin Chem Biol 14:71–79
15. Hong GS, Antaris AL, Dai HJ (2017) Near-infrared fluorophores for biomedical imaging. Nat Biomed Eng 1
16. Hong G, Lee JC, Robinson JT, Raaz U, Xie L, Huang NF, Cooke JP, Dai H (2012) Multifunctional in vivo vascular imaging using near-infrared II fluorescence. Nat Med 18:1841–1846
17. Smith AM, Mancini MC, Nie SM (2009) BIOIMAGING second window for in vivo imaging. Nat Nanotechnol 4:710–711
18. Hong GS, Diao S, Chang JL, Antaris AL, Chen CX, Zhang B, Zhao S, Atochin DN, Huang PL, Andreasson KI, Kuo CJ, Dai HJ (2014) Through-skull fluorescence imaging of the brain in a new near-infrared window. Nat Photonics 8:723–730
19. Zhang Y, Hong GS, Zhang YJ, Chen GC, Li F, Dai HJ, Wang QB (2012) Ag2S quantum dot: a bright and biocompatible fluorescent nanoprobe in the second near-infrared window. ACS Nano 6:3695–3702
20. Won N, Jeong S, Kim K, Kwag J, Park J, Kim SG, Kim S (2012) Imaging depths of near-infrared quantum dots in first and second optical windows. Mol Imaging 11:338–352
21. Li CY, Zhang YJ, Wang M, Zhang Y, Chen GC, Li L, Wu DM, Wang QB (2014) In vivo real-time visualization of tissue blood flow and angiogenesis using Ag2S quantum dots in the NIR-II window. Biomaterials 35:393–400
22. Bruns OT, Bischof TS, Harris DK, Franke D, Shi Y, Riedemann L, Bartelt A, Jaworski FB, Carr JA, Rowlands CJ, Wilson MWB, Chen O, Wei H, Hwang GW, Montana DM, Coropceanu I, Achorn OB, Kloepper J, Heeren J, So PTC, Fukumura D, Jensen KF, Jain RK, Bawendi MG (2017) Next-generation in vivo optical imaging with short-wave infrared quantum dots. Nat Biomed Eng 1
23. Derfus AM, Chan WCW, Bhatia SN (2004) Probing the cytotoxicity of semiconductor quantum dots. Nano Lett 4:11–18

24. Xu G, Zeng S, Zhang B, Swihart MT, Yong KT, Prasad PN (2016) New generation cadmium-free quantum dots for biophotonics and nanomedicine. Chem Rev 116:12234–12327
25. Dabbousi BO, RodriguezViejo J, Mikulec FV, Heine JR, Mattoussi H, Ober R, Jensen KF, Bawendi MG (1997) (CdSe)ZnS core-shell quantum dots: synthesis and characterization of a size series of highly luminescent nanocrystallites. J Phys Chem B 101:9463–9475
26. Choi HS, Liu W, Misra P, Tanaka E, Zimmer JP, Ipe BI, Bawendi MG, Frangioni JV (2007) Renal clearance of quantum dots. Nat Biotechnol 25:1165–1170
27. Zhu XJ, Su QQ, Feng W, Li FY (2017) Anti-stokes shift luminescent materials for bio-applications. Chem Soc Rev 46:1025–1039
28. Zagorovsky K, Chan WCW (2013) BIOIMAGING illuminating the deep. Nat Mater 12:285–287
29. Yu JH, Kwon SH, Petrasek Z, Park OK, Jun SW, Shin K, Choi M, Park YI, Park K, Na HB, Lee N, Lee DW, Kim JH, Schwille P, Hyeon T (2013) High-resolution three-photon biomedical imaging using doped ZnS nanocrystals. Nat Mater 12:359–366
30. Subha R, Nalla V, Yu JH, Jun SW, Shin K, Hyeon T, Vijayan C, Ji W (2013) Efficient photoluminescence of Mn2+-doped ZnS quantum dots excited by two-photon absorption in near-infrared window II. J Phys Chem C 117:20905–20911
31. Chatteriee DK, Rufalhah AJ, Zhang Y (2008) Upconversion fluorescence imaging of cells and small animals using lanthanide doped nanocrystals. Biomaterials 29:937–943
32. Cheng L, Yang K, Zhang S, Shao M, Lee S, Liu Z (2010) Highly-sensitive multiplexed in vivo imaging using pegylated upconversion nanoparticles. Nano Res 3:722–732
33. Chen G, Qiu H, Prasad PN, Chen X (2014) Upconversion nanoparticles: design, nanochemistry, and applications in theranostics. Chem Rev 114:5161–5214
34. Park YI, Lee KT, Suh YD, Hyeon T (2015) Upconverting nanoparticles: a versatile platform for wide-field two-photon microscopy and multi-modal in vivo imaging. Chem Soc Rev 44:1302–1317
35. Wang F, Han Y, Lim CS, Lu YH, Wang J, Xu J, Chen HY, Zhang C, Hong MH, Liu XG (2010) Simultaneous phase and size control of upconversion nanocrystals through lanthanide doping. Nature 463:1061–1065
36. Wang F, Liu XG (2008) Upconversion multicolor fine-tuning: visible to near-infrared emission from lanthanide-doped NaYF4 nanoparticles. J Am Chem Soc 130:5642–5643
37. Auzel F (2004) Upconversion and anti-stokes processes with f and d ions in solids. Chem Rev 104:139–173
38. Wang F, Deng RR, Wang J, Wang QX, Han Y, Zhu HM, Chen XY, Liu XG (2011) Tuning upconversion through energy migration in core-shell nanoparticles. Nat Mater 10:968–973
39. Meshulach D, Silberberg Y (1998) Coherent quantum control of two-photon transitions by a femtosecond laser pulse. Nature 396:239–242
40. Liu Q, Feng W, Yang T, Yi T, Li F (2013) Upconversion luminescence imaging of cells and small animals. Nat Protoc 8:2033–2044
41. Nam SH, Bae YM, Park YI, Kim JH, Kim HM, Choi JS, Lee KT, Hyeon T, Suh YD (2011) Long-term real-time tracking of lanthanide ion doped upconverting nanoparticles in living cells. Angew Chem-Int Edit 50:6093–6097
42. Liu Q, Sun Y, Yang T, Feng W, Li C, Li F (2011) Sub-10 nm hexagonal lanthanide-doped NaLuF4 upconversion nanocrystals for sensitive bioimaging in vivo. J Am Chem Soc 133:17122–17125
43. Zhan QQ, Qian J, Liang HJ, Somesfalean G, Wang D, He SL, Zhang ZG, Andersson-Engels S (2011) Using 915 nm laser excited Tm3+/Er3+/Ho3+-doped NaYbF4 upconversion nanoparticles for in vitro and deeper in vivo bioimaging without overheating irradiation. ACS Nano 5:3744–3757
44. Wang YF, Liu GY, Sun LD, Xiao JW, Zhou JC, Yan CH (2013) Nd3+-sensitized upconversion nanophosphors: efficient in vivo bioimaging probes with minimized heating effect. ACS Nano 7:7200–7206

45. Chen GY, Shen J, Ohulchanskyy TY, Patel NJ, Kutikov A, Li ZP, Song J, Pandey RK, Agren H, Prasad PN, Han G (2012) Alpha-NaYbF4:Tm(3+)/CaF2 core/shell nanoparticles with efficient near-infrared to near-infrared upconversion for high-contrast deep tissue bioimaging. ACS Nano 6:8280–8287
46. Wang L, Zhu SJ, Wang HY, Qu SN, Zhang YL, Zhang JH, Chen QD, Xu HL, Han W, Yang B, Sun HB (2014) Common origin of green luminescence in carbon nanodots and graphene quantum dots. ACS Nano 8:2541–2547
47. Zhu SJ, Song YB, Zhao XH, Shao JR, Zhang JH, Yang B (2015) The photoluminescence mechanism in carbon dots (graphene quantum dots, carbon nanodots, and polymer dots): current state and future perspective. Nano Res 8:355–381
48. Lim SY, Shen W, Gao ZQ (2015) Carbon quantum dots and their applications. Chem Soc Rev 44:362–381
49. Sun YP, Zhou B, Lin Y, Wang W, Fernando KAS, Pathak P, Meziani MJ, Harruff BA, Wang X, Wang HF, Luo PJG, Yang H, Kose ME, Chen BL, Veca LM, Xie SY (2006) Quantum-sized carbon dots for bright and colorful photoluminescence. J Am Chem Soc 128:7756–7757
50. Cao L, Wang X, Meziani MJ, Lu FS, Wang HF, Luo PJG, Lin Y, Harruff BA, Veca LM, Murray D, Xie SY, Sun YP (2007) Carbon dots for multiphoton bioimaging. J Am Chem Soc 129:11318–11319
51. Baker SN, Baker GA (2010) Luminescent carbon nanodots: emergent nanolights. Angew Chem-Int Edit 49:6726–6744
52. Wang X, Cao L, Yang ST, Lu FS, Meziani MJ, Tian LL, Sun KW, Bloodgood MA, Sun YP (2010) Bandgap-like strong fluorescence in functionalized carbon nanoparticles. Angew Chem-Int Edit 49:5310–5314
53. Cao L, Yang ST, Wang X, Luo PJG, Liu JH, Sahu S, Liu YM, Sun YP (2012) Competitive performance of carbon "quantum" dots in optical bioimaging. Theranostics 2:295–301
54. Liu S, Tian JQ, Wang L, Zhang YW, Qin XY, Luo YL, Asiri AM, Al-Youbi AO, Sun XP (2012) Hydrothermal treatment of grass: a low-cost, green route to nitrogen-doped, carbon-rich, photoluminescent polymer nanodots as an effective fluorescent sensing platform for label-free detection of cu(II) ions. Adv Mater 24:2037–2041
55. Zhang J, Yuan Y, Liang GL, Yu SH (2015) Scale-up synthesis of fragrant nitrogen-doped carbon dots from bee pollens for bioimaging and catalysis. Adv Sci 2(4):1500002
56. Pal T, Mohiyuddin S, Packirisamy G (2018) Facile and green synthesis of multicolor fluorescence carbon dots from curcumin: in vitro and in vivo bioimaging and other applications. ACS Omega 3:831–843
57. Park JH, Gu L, von Maltzahn G, Ruoslahti E, Bhatia SN, Sailor MJ (2009) Biodegradable luminescent porous silicon nanoparticles for in vivo applications. Nat Mater 8:331–336
58. Gu L, Hall DJ, Qin Z, Anglin E, Joo J, Mooney DJ, Howell SB, Sailor MJ (2013) In vivo time-gated fluorescence imaging with biodegradable luminescent porous silicon nanoparticles. Nat Commun 4:2326
59. Cullis AG, Canham LT, Calcott PDJ (1997) The structural and luminescence properties of porous silicon. J Appl Phys 82:909–965
60. Tasciotti E, Liu X, Bhavane R, Plant K, Leonard AD, Price BK, Cheng MM-C, Decuzzi P, Tour JM, Robertson F, Ferrari M (2008) Mesoporous silicon particles as a multistage delivery system for imaging and therapeutic applications. Nat Nanotechnol 3:151
61. Karaman DS, Sarparanta MP, Rosenholm JM, Airaksinen AJ (2018) Multimodality imaging of silica and silicon materials in vivo. Adv Mater 30:e1703651
62. Li W, Liu Z, Fontana F, Ding Y, Liu D, Hirvonen JT, Santos HA (2018) Tailoring porous silicon for biomedical applications: from drug delivery to cancer immunotherapy. Adv Mater 30:e1703740
63. Eustis S, El-Sayed MA (2006) Why gold nanoparticles are more precious than pretty gold: noble metal surface plasmon resonance and its enhancement of the radiative and nonradiative properties of nanocrystals of different shapes. Chem Soc Rev 35:209–217

64. Zheng J, Zhang CW, Dickson RM (2004) Highly fluorescent, water-soluble, size-tunable gold quantum dots. Phys Rev Lett 93(7):077402
65. Lin CAJ, Yang TY, Lee CH, Huang SH, Sperling RA, Zanella M, Li JK, Shen JL, Wang HH, Yeh HI, Parak WJ, Chang WH (2009) Synthesis, characterization, and bioconjugation of fluorescent gold nanoclusters toward biological labeling applications. ACS Nano 3:395–401
66. Negishi Y, Takasugi Y, Sato S, Yao H, Kimura K, Tsukuda T (2004) Magic-numbered Au-n clusters protected by glutathione monolayers (n=18, 21, 25, 28, 32, 39): isolation and spectroscopic characterization. J Am Chem Soc 126:6518–6519
67. Negishi Y, Nobusada K, Tsukuda T (2005) Glutathione-protected gold clusters revisited: bridging the gap between gold(I)-thiolate complexes and thiolate-protected gold nanocrystals. J Am Chem Soc 127:5261–5270
68. Wang GL, Huang T, Murray RW, Menard L, Nuzzo RG (2005) Near-IR luminescence of monolayer-protected metal clusters. J Am Chem Soc 127:812–813
69. Palmal S, Basiruddin SK, Maity AR, Ray SC, Jana NR (2013) Thiol-directed synthesis of highly fluorescent gold clusters and their conversion into stable imaging nanoprobes. Chem-Eur J 19:943–949
70. Xie JP, Zheng YG, Ying JY (2009) Protein-directed synthesis of highly fluorescent gold nanoclusters. J Am Chem Soc 131:888–889
71. Vosch T, Antoku Y, Hsiang JC, Richards CI, Gonzalez JI, Dickson RM (2007) Strongly emissive individual DNA-encapsulated Ag nanoclusters as single-molecule fluorophores. Proc Natl Acad Sci U S A 104:12616–12621
72. Wu Z, Jin R (2010) On the ligand's role in the fluorescence of gold nanoclusters. Nano Lett 10:2568–2573
73. Duan HW, Nie SM (2007) Etching colloidal gold nanocrystals with hyperbranched and multivalent polymers: a new route to fluorescent and water-soluble atomic clusters. J Am Chem Soc 129:2412–2413
74. Wang HH, Lin CAJ, Lee CH, Lin YC, Tseng YM, Hsieh CL, Chen CH, Tsai CH, Hsieh CT, Shen JL, Chan WH, Chang WH, Yeh HI (2011) Fluorescent gold nanoclusters as a biocompatible marker for in vitro and in vivo tracking of endothelial cells. ACS Nano 5:4337–4344
75. Wu X, He X, Wang K, Xie C, Zhou B, Qing Z (2010) Ultrasmall near-infrared gold nanoclusters for tumor fluorescence imaging in vivo. Nanoscale 2:2244–2249
76. Yu MX, Zhou JC, Du BJ, Ning XH, Authement C, Gandee L, Kapur P, Hsieh JT, Zheng J (2016) Noninvasive staging of kidney dysfunction enabled by renal-clearable luminescent gold nanoparticles. Angew Chem-Int Edit 55:2787–2791
77. Mochalin VN, Shenderova O, Ho D, Gogotsi Y (2012) The properties and applications of nanodiamonds. Nat Nanotechnol 7:11–23
78. Gruber A, Drabenstedt A, Tietz C, Fleury L, Wrachtrup J, vonBorczyskowski C (1997) Scanning confocal optical microscopy and magnetic resonance on single defect centers. Science 276:2012–2014
79. Yu SJ, Kang MW, Chang HC, Chen KM, Yu YC (2005) Bright fluorescent nanodiamonds: no photobleaching and low cytotoxicity. J Am Chem Soc 127:17604–17605
80. Tisler J, Balasubramanian G, Naydenov B, Kolesov R, Grotz B, Reuter R, Boudou JP, Curmi PA, Sennour M, Thorel A, Borsch M, Aulenbacher K, Erdmann R, Hemmer PR, Jelezko F, Wrachtrup J (2009) Fluorescence and spin properties of defects in single digit nanodiamonds. ACS Nano 3:1959–1965
81. Fu CC, Lee HY, Chen K, Lim TS, Wu HY, Lin PK, Wei PK, Tsao PH, Chang HC, Fann W (2007) Characterization and application of single fluorescent nanodiamonds as cellular biomarkers. Proc Natl Acad Sci U S A 104:727–732
82. Hsiao WW, Hui YY, Tsai PC, Chang HC (2016) Fluorescent nanodiamond: a versatile tool for long-term cell tracking, super-resolution imaging, and nanoscale temperature sensing. Acc Chem Res 49:400–407

83. Tzeng YK, Faklaris O, Chang BM, Kuo Y, Hsu JH, Chang HC (2011) Superresolution imaging of albumin-conjugated fluorescent nanodiamonds in cells by stimulated emission depletion. Angew Chem-Int Edit 50:2262–2265
84. Haziza S, Mohan N, Loe-Mie Y, Lepagnol-Bestel AM, Massou S, Adam MP, Le XL, Viard J, Plancon C, Daudin R, Koebel P, Dorard E, Rose C, Hsieh FJ, Wu CC, Potier B, Herault Y, Sala C, Corvin A, Allinquant B, Chang HC, Treussart F, Simonneau M (2017) Fluorescent nanodiamond tracking reveals intraneuronal transport abnormalities induced by brain-disease-related genetic risk factors. Nat Nanotechnol 12:322–328
85. Wu TJ, Tzeng YK, Chang WW, Cheng CA, Kuo Y, Chien CH, Chang HC, Yu J (2013) Tracking the engraftment and regenerative capabilities of transplanted lung stem cells using fluorescent nanodiamonds. Nat Nanotechnol 8:682–689
86. Lecuyer T, Teston E, Ramirez-Garcia G, Maldiney T, Viana B, Seguin J, Mignet N, Scherman D, Richard C (2016) Chemically engineered persistent luminescence nanoprobes for bioimaging. Theranostics 6:2488–2524
87. le Masne de Chermont Q, Chaneac C, Seguin J, Pelle F, Maitrejean S, Jolivet JP, Gourier D, Bessodes M, Scherman D (2007) Nanoprobes with near-infrared persistent luminescence for in vivo imaging. Proc Natl Acad Sci U S A 104:9266–9271
88. Maldiney T, Bessiere A, Seguin J, Teston E, Sharma SK, Viana B, Bos AJJ, Dorenbos P, Bessodes M, Gourier D, Scherman D, Richard C (2014) The in vivo activation of persistent nanophosphors for optical imaging of vascularization, tumours and grafted cells. Nat Mater 13:418–426
89. Altinoglu EI, Russin TJ, Kaiser JM, Barth BM, Eklund PC, Kester M, Adair JH (2008) Near-infrared emitting fluorophore-doped calcium phosphate nanoparticles for in vivo imaging of human breast cancer. ACS Nano 2:2075–2084
90. Tabakovic A, Kester M, Adair JH (2012) Calcium phosphate-based composite nanoparticles in bioimaging and therapeutic delivery applications. Wiley Interdiscip Rev-Nanomed Nanobiotechnol 4:96–112
91. Frangioni JV (2003) In vivo near-infrared fluorescence imaging. Curr Opin Chem Biol 7:626–634
92. Barth BM, Sharma R, Altinoglu EI, Morgan TT, Shanmugavelandy SS, Kaiser JM, McGovern C, Matters GL, Smith JP, Kester M, Adair JH (2010) Bioconjugation of calcium phosphosilicate composite nanoparticles for selective targeting of human breast and pancreatic cancers in vivo. ACS Nano 4:1279–1287
93. Tarn D, Ashley CE, Xue M, Carnes EC, Zink JI, Brinker CJ (2013) Mesoporous silica nanoparticle nanocarriers: biofunctionality and biocompatibility. Acc Chem Res 46:792–801
94. Cho EB, Volkov DO, Sokolov I (2011) Ultrabright fluorescent silica mesoporous silica nanoparticles: control of particle size and dye loading. Adv Funct Mater 21:3129–3135
95. Ow H, Larson DR, Srivastava M, Baird BA, Webb WW, Wiesner U (2005) Bright and stable core-shell fluorescent silica nanoparticles. Nano Lett 5:113–117
96. Benezra M, Penate-Medina O, Zanzonico PB, Schaer D, Ow H, Burns A, DeStanchina E, Longo V, Herz E, Iyer S, Wolchok J, Larson SM, Wiesner U, Bradbury MS (2011) Multimodal silica nanoparticles are effective cancer-targeted probes in a model of human melanoma. J Clin Invest 121:2768–2780
97. Phillips E, Penate-Medina O, Zanzonico PB, Carvajal RD, Mohan P, Ye YP, Humm J, Gonen M, Kalaigian H, Schoder H, Strauss HW, Larson SM, Wiesner U, Bradbury MS (2014) Clinical translation of an ultrasmall inorganic optical-PET imaging nanoparticle probe. Sci Transl Med 6:260ra149
98. Sharma P, Bengtsson NE, Walter GA, Sohn HB, Zhou GY, Iwakuma N, Zeng HD, Grobmyer SR, Scott EW, Moudgil BM (2012) Gadolinium-doped silica nanoparticles encapsulating indocyanine green for near infrared and magnetic resonance imaging. Small 8:2856–2868

99. Lee CH, Cheng SH, Wang YJ, Chen YC, Chen NT, Souris J, Chen CT, Mou CY, Yang CS, Lo LW (2009) Near-infrared mesoporous silica nanoparticles for optical imaging: characterization and in vivo biodistribution. Adv Funct Mater 19:215–222
100. Ferrauto G, Carniato F, Di Gregorio E, Tei L, Botta M, Aime S (2017) Large photoacoustic effect enhancement for ICG confined inside MCM-41 mesoporous silica nanoparticles. Nanoscale 9:99–103
101. Kang J, Kim D, Wang J, Han Y, Zuidema JM, Hariri A, Park JH, Jokerst JV, Sailor MJ (2018) Enhanced performance of a molecular photoacoustic imaging agent by encapsulation in mesoporous silicon nanoparticles. Adv Mater 30(27):e1800512